Supplement of Atmos. Chem. Phys., 26, 789–807, 2026
https://doi.org/10.5194/acp-26-789-2026-supplement

Atmospheric Chemistry and Physics
Open Access

Supplement of

Measurement report: Altitudinal shift of ozone regimes in a mountainous background region

Yuan Yang et al.

Correspondence to: Yonghong Wang (yonghongwang@rcees.ac.cn)

S1 Raincloud plots

Raincloud plots are an innovative and comprehensive data visualization tool designed to provide a complete, transparent view of dataset distributions. As the name suggests, they combine three key elements: a "cloud" (a density plot or half-violin showing the full data distribution), "rain" (individual data points shown as jittered points, revealing the raw data), and a "box" (a compact boxplot displaying key summary statistics like the median and interquartile range). This trio of components in a single plot allows researchers to simultaneously see the overall shape of the data, its precise summary metrics, and every individual observation, thereby overcoming the limitations of traditional charts that often hide underlying data patterns or outliers.

The primary strength of raincloud plots is their robustness and transparency, which helps to prevent misinterpretation and promotes rigorous, reproducible data analysis. They are considered a multi-platform tool because robust, open-source code implementations are readily available for popular data science environments, most notably R (using packages like ggplot2 and ggdist), Python (through libraries such as Matplotlib, Seaborn, and PtitPrince), and even MATLAB. This cross-platform accessibility has made them widely adopted across fields like psychology, neuroscience, and the life sciences, where understanding full data distributions is critical. By elegantly integrating detailed distributional information with raw data visualization, raincloud plots have become a standard for modern, honest, and effective statistical communication.

Table S1. The correlation coefficients (R^2), relative error and Method detection limit (MDL) of measured VOC compounds and their mixing ratios (mean concentration ± standard deviation) at the mountain foot, mountainside, and mountaintop sites during the observational campaign (March-August 2024).

Species	R^2	relative error	MDL (nmol/mol)	Mountain foot (ppb)	Mountainside (ppb)	Mountaintop (ppb)
Ethane	0.999766	-2.80%	0.09	1.54±0.73	1.37±0.73	1.48±1.21
Ethylene	0.999481	-1.73%	0.07	1.06±0.75	0.35±0.14	2.23±3.77
Propane	0.999780	0.00%	0.09	0.64±0.35	0.47±0.30	1.96±16.31
Propylene	0.999783	6.93%	0.05	0.36±0.26	0.06±0.02	0.62±1.93
Isobutane	0.999806	-0.67%	0.19	0.31±0.11	0.18±0.05	0.63±3.34
n-Butane	0.999841	-0.27%	0.10	0.31±0.15	0.18±0.08	0.77±4.37
Acetylene	0.999916	1.47%	0.04	0.34±0.53	0.19±0.15	0.34±0.18
trans-2-Butene	0.999794	1.87%	0.03	0.16±0.10	0.18±0.14	0.24±0.48
1-Butene	0.999847	-0.20%	0.03	0.44±0.24	0.13±0.02	0.25±0.31
cis-2-Butene	0.999810	1.73%	0.01	0.83±0.53	0.10±0.01	0.14±0.10
Isopentane	0.999685	2.67%	0.02	0.31±1.09	0.12±0.03	0.25±1.74
Cyclopentane	0.999897	-3.07%	0.04	0.33±0.16	0.10±0.01	0.16±0.15
n-Pentane	0.999809	1.67%	0.01	0.20±0.25	0.12±0.03	0.19±0.58
trans-2-Pentene	0.999786	2.13%	0.01	0.11±0.08	0.12±0.02	0.17±0.41
1-Pentene	0.999767	2.93%	0.02	0.16±0.07	0.11±0.01	0.14±0.13
cis-2-Pentene	0.999771	4.33%	0.01	0.11±0.08	0.11±0.01	0.19±0.27
2,2-Dimethylbutane	0.999750	3.67%	0.03	0.06±0.08	0.05±0.04	0.06±0.10
2,3-Dimethylbutane	0.999762	4.13%	0.02	0.41±0.31	0.31±0.34	0.61±1.19
2-Methylpentane	0.999345	9.67%	0.02	0.36±0.49	0.25±0.60	0.40±1.13
3-Methylpentane	0.999475	7.60%	0.01	0.15±0.20	0.09±0.01	0.14±0.45
Methylcyclopentane	0.999730	4.67%	0.01	0.16±0.14	0.10±0.01	0.12±0.01
n-Hexane	0.999662	2.73%	0.01	0.17±0.25	0.12±0.07	0.15±0.24
Isoprene	0.999728	4.53%	0.01	0.49±0.65	0.29±0.27	0.26±0.20
1-Hexene	0.999783	4.60%	0.02	0.11±0.04	0.11±0.07	0.13±0.08
2,4-Dimethylpentane	0.999712	1.53%	0.02	0.17±0.09	0.12±0.14	0.13±0.20
Benzene	0.999636	11.60%	0.03	0.17±0.11	0.20±0.06	0.21±0.07
Cyclohexane	0.999501	7.60%	0.05	0.04±0.10	0.07±0.01	0.15±0.01
2-Methylhexane	0.999338	4.13%	0.03	0.11±0.33	0.12±0.02	0.21±0.64
2,3-Dimethylpentane	0.999551	0.93%	0.03	0.14±0.29	0.14±0.01	0.17±0.15
3-Methylhexane	0.999507	-2.27%	0.03	0.10±0.27	0.13±0.01	0.16±0.17
2,2,4-Trimethylpentane	0.999424	5.07%	0.03	0.09±0.12	0.11±0.01	0.18±0.34
n-Heptane	0.999490	4.60%	0.03	0.11±0.38	0.13±0.00	0.20±0.40
Methylcyclohexane	0.999532	4.20%	0.04	0.09±0.06	0.12±0.01	0.16±0.10
2,3,4-Trimethylpentane	0.999445	4.40%	0.03	0.15±0.06	0.14±0.02	0.19±0.12
Toluene	0.999398	7.67%	0.03	3.42±4.61	0.29±0.07	0.35±0.65
2-Methylheptane	0.999440	2.93%	0.04	1.27±2.58	0.11±0.00	0.19±0.29
3-Methylheptane	0.999347	2.47%	0.05	0.12±0.06	0.12±0.01	0.18±0.07
n-Octane	0.999304	4.07%	0.07	0.08±0.28	0.12±0.00	0.17±0.07
Ethylbenzene	0.999277	5.47%	0.07	0.12±0.46	0.14±0.01	0.20±0.22

m/p-Xylene	0.999278	2.73%	0.06	0.28±1.68	0.14±0.02	0.25±0.30
Styrene	0.998736	9.67%	0.06	0.18±0.13	0.23±0.02	0.36±0.08
o-Xylene	0.999266	5.53%	0.07	0.21±0.68	0.14±0.04	0.27±0.70
n-Nonane	0.999284	4.73%	0.09	0.13±0.10	0.10±0.05	0.17±0.05
Isopropylbenzene	0.999240	7.00%	0.07	0.12±0.11	0.02±0.00	0.14±0.05
n-Propylbenzene	0.998988	6.80%	0.09	0.30±0.21	0.20±0.05	0.42±0.07
m-Ethyltoluene	0.998785	8.13%	0.10	0.22±0.23	0.06±0.07	0.34±0.85
p-Ethyltoluene	0.998774	7.47%	0.09	0.23±0.15	0.08±0.06	0.28±0.21
1,3,5-Trimethylbenzene	0.999069	3.07%	0.09	0.22±0.20	0.04±0.05	0.16±0.09
o-Ethyltoluene	0.999552	-4.87%	0.11	0.31±0.12	0.19±0.05	0.18±0.09
1,2,4-Trimethylbenzene	0.998876	5.87%	0.08	0.25±0.24	0.23±0.04	0.42±0.52
n-Decane	0.998923	1.00%	0.08	0.18±0.01	0.05±0.00	0.21±0.21
1,2,3-Trimethylbenzene	0.998522	11.27%	0.11	0.21±0.10	0.19±0.04	0.28±0.20
m-Diethylbenzene	0.998526	10.27%	0.07	0.23±0.07	0.21±0.04	0.22±0.12
p-Diethylbenzene	0.998269	11.80%	0.08	0.28±0.09	0.11±0.13	0.19±0.13
n-Undecane	0.998643	5.00%	0.07	0.33±0.15	0.24±0.11	0.20±0.07
n-Dodecane	0.998079	11.53%	0.13	0.25±0.06	0.23±0.04	0.33±0.04

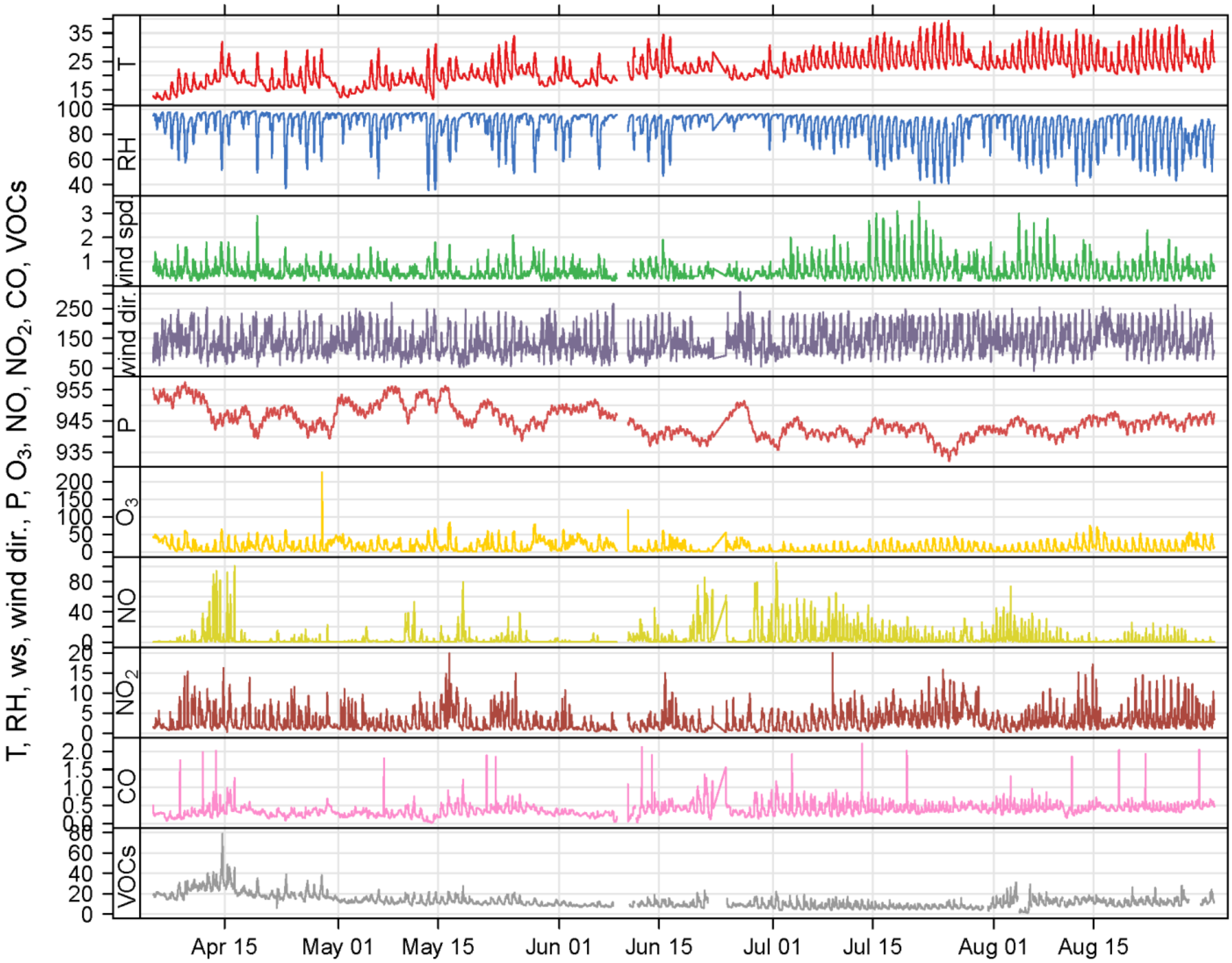

Figure S1. Time series of ambient temperature (T), relative humidity (RH), wind speed (wind spd.), wind direction (wind dir.), atmospheric pressure (P), O_3, NO, NO_2, CO, VOCs from 5 April 2024 to 31 August 2024 at mountain-foot O_3 and precursor monitoring station. Gaps in the data series indicate either instrument unavailability during calibration/maintenance or measured values below the method detection limit (MDL).

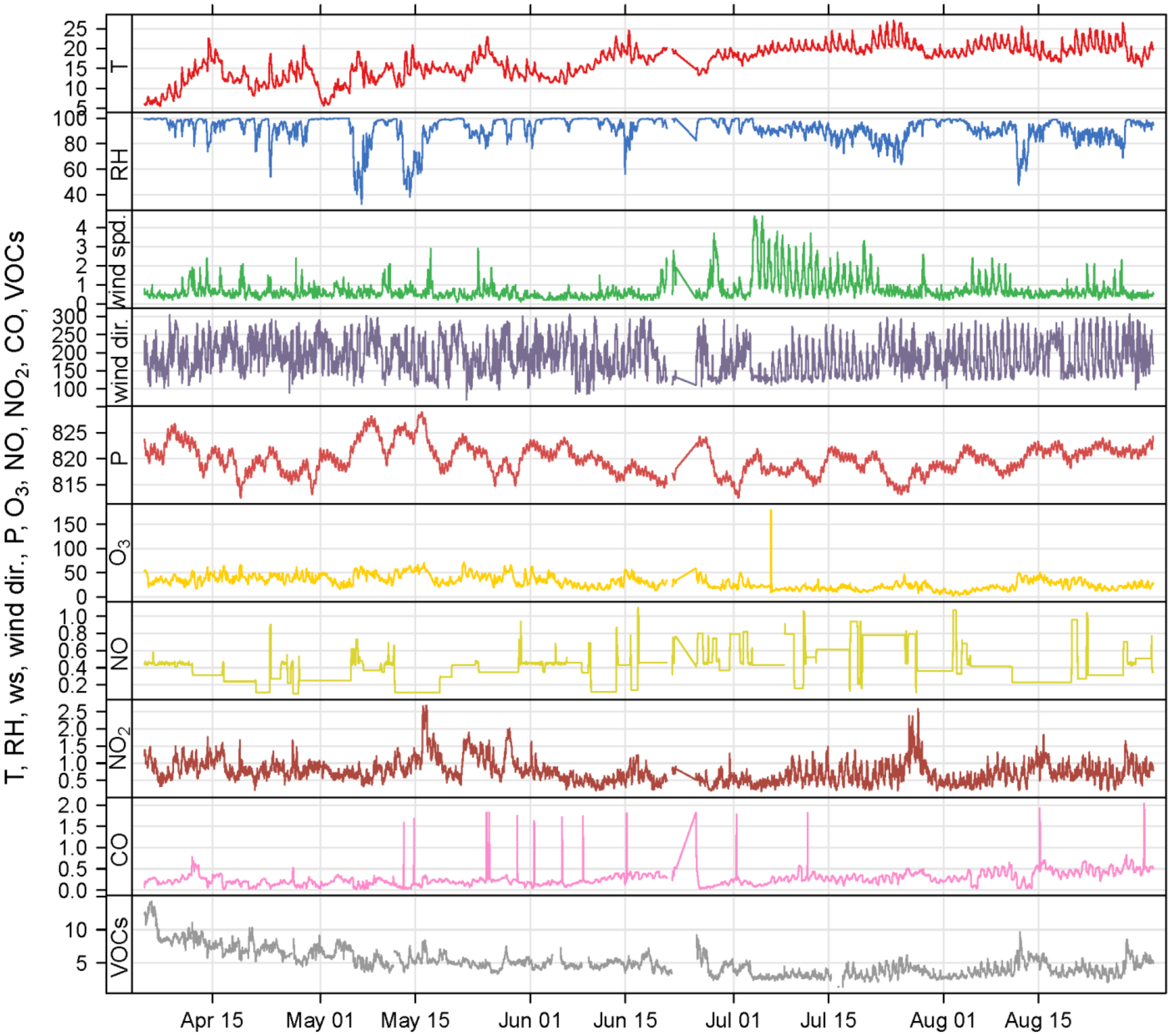

Figure S2. Time series of ambient temperature (T), relative humidity (RH), wind speed (wind spd.), wind direction (wind dir.), atmospheric pressure (P), O_3, NO, NO_2, CO, VOCs from 5 April 2024 to 31 August 2024 at mountainside O_3 and precursor monitoring station. Discontinuities correspond to periods of data unavailability during instrument calibration/maintenance or concentrations below the method detection limit (MDL).

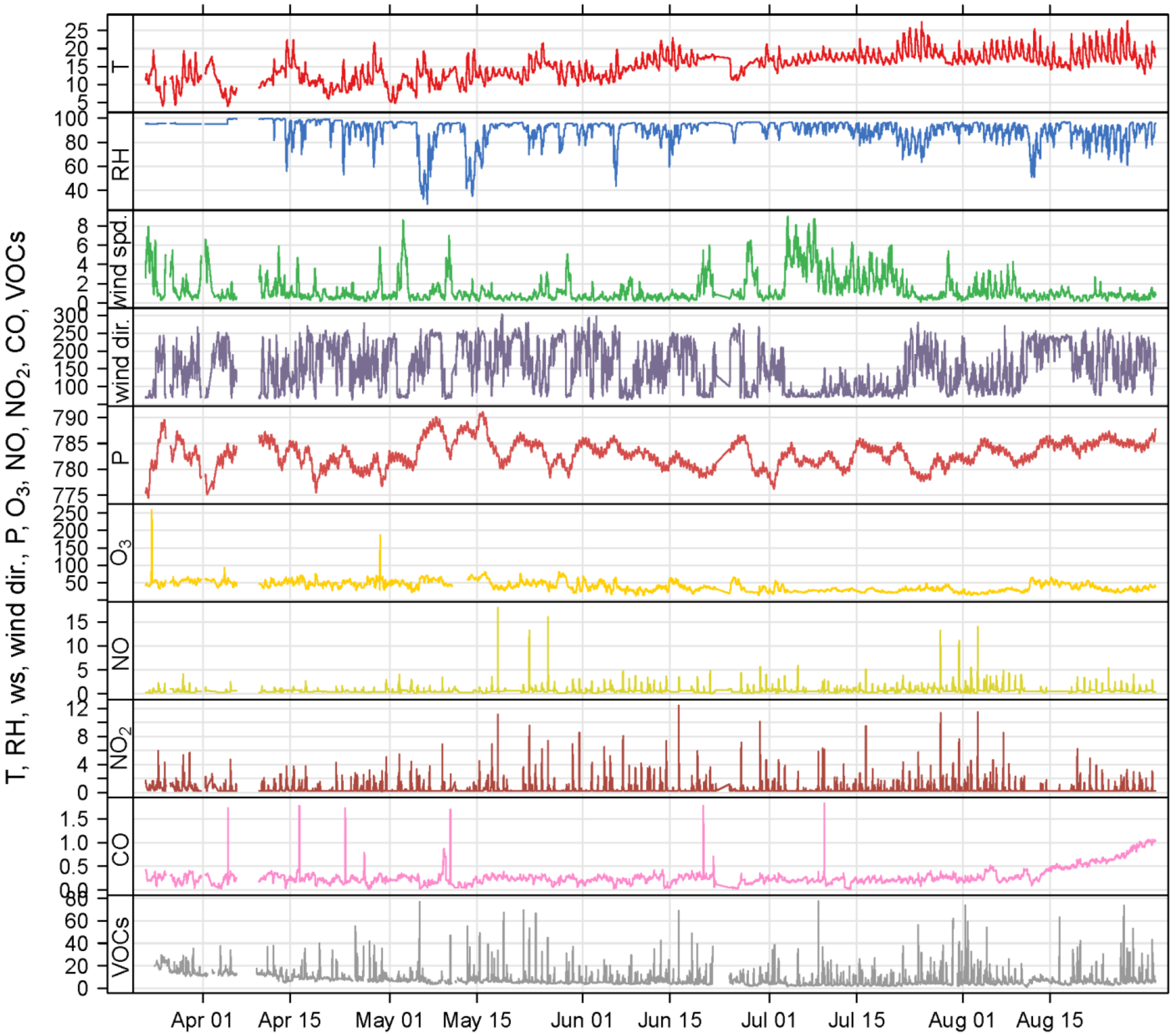

Figure S3. Time series of ambient temperature (T), relative humidity (RH), wind speed (wind spd.), wind direction (wind dir.), atmospheric pressure (P), O_3, NO, NO_2, CO, VOCs from 5 April 2024 to 31 August 2024 at mountaintop O_3 and precursor monitoring station. Data discontinuities arise either from instrument unavailability during calibration/maintenance activities or from measured values falling below the method detection limit (MDL).

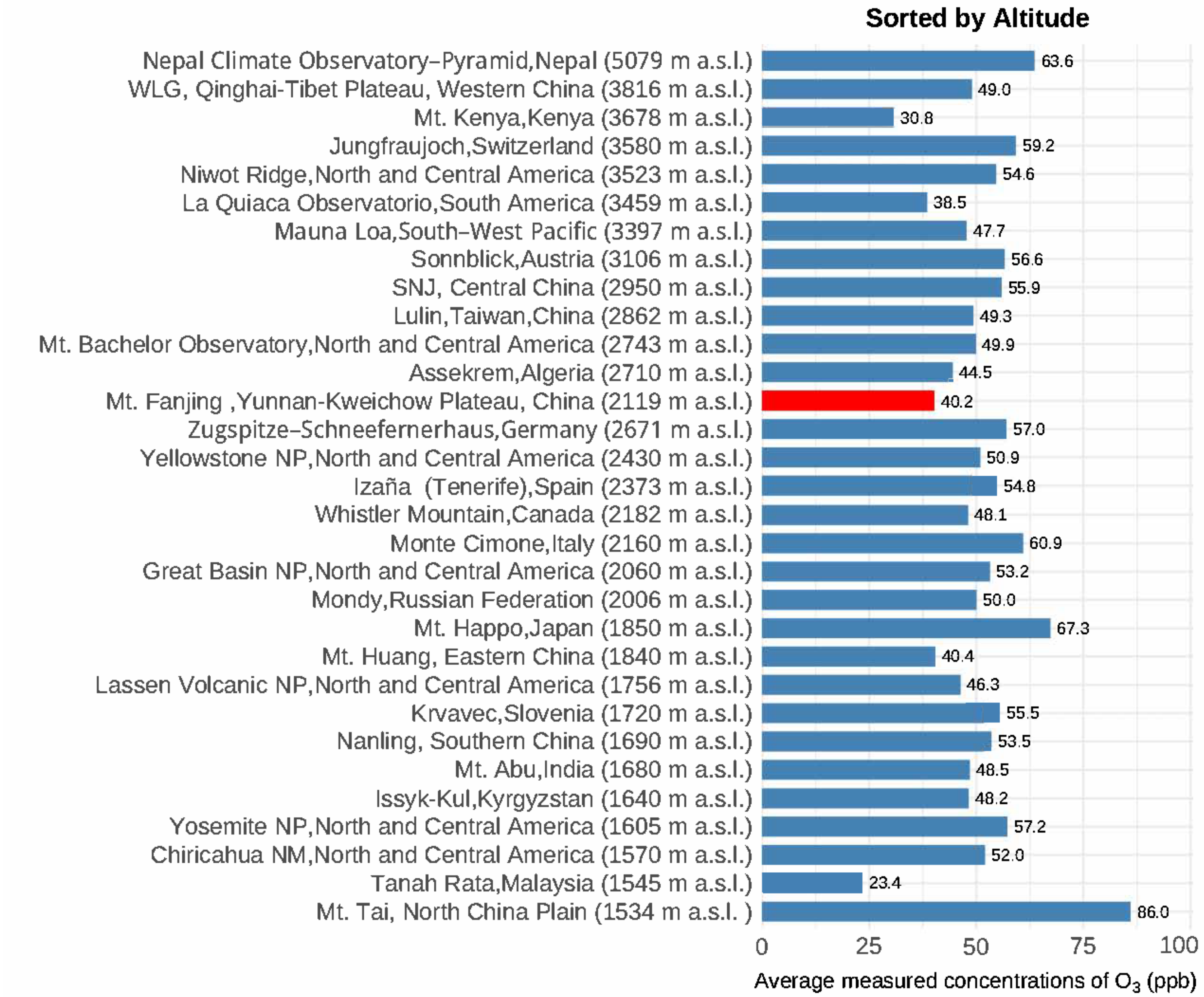

Figure S4. Comparison of O_3 concentrations at Mt. Fanjing summit (2024, March–August) with those observed at mountain sites across the globe. The data is organized in descending order of Altitude, with each site listed alongside its elevation in meters above sea level (m a.s.l.). All average values are reported in ppb. Data were compiled from published literature (Okamoto and Tanimoto, 2016; Li et al., 2007; Lyu et al., 2021; Xu et al., 2016; Gong et al., 2018; Sun et al., 2016).

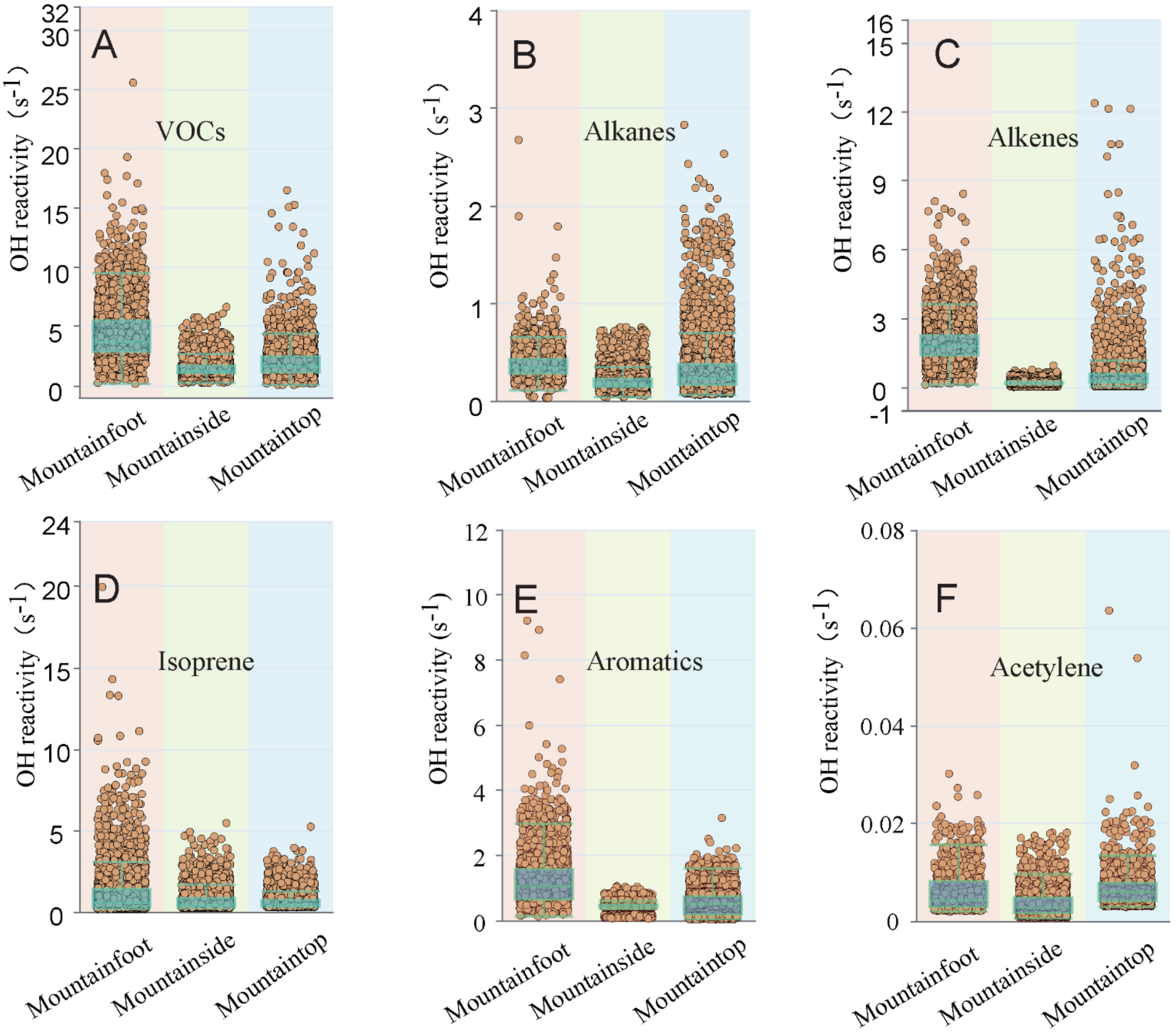

Figure S5. Comprehensive characterization of speciated OH reactivity for PAMS species. Horizontally jittered data points depict raw measurements, revealing underlying data density and distributional characteristics. Transparent tukey-style boxplot summarize key statistical descriptors. The box represents the interquartile range (IQR) of the data, encompassing the range between the upper quartile (Q3) and the lower quartile (Q1). The horizontal line within the box denotes the median value. The whiskers extend to indicate the data range, typically corresponding to 1.5 times the IQR. The speciated OH reactivity, which represents the inverse of the OH radical lifetime, is quantitatively determined by the summation of products between the bimolecular rate coefficients for OH reactions and the corresponding concentrations of individual reactive species(Yang et al., 2016; Ling et al., 2014; Whalley et al., 2016). The OH reaction rate coefficients were obtained from the Master Chemical Mechanism (MCM version 3.3.1; accessible at https://mcm.york.ac.uk, last accessed on 19 May 2025), a comprehensive atmospheric chemical mechanism widely employed in tropospheric chemistry research, and the literature (Atkinson and Arey, 2003; Atkinson et al., 2006).

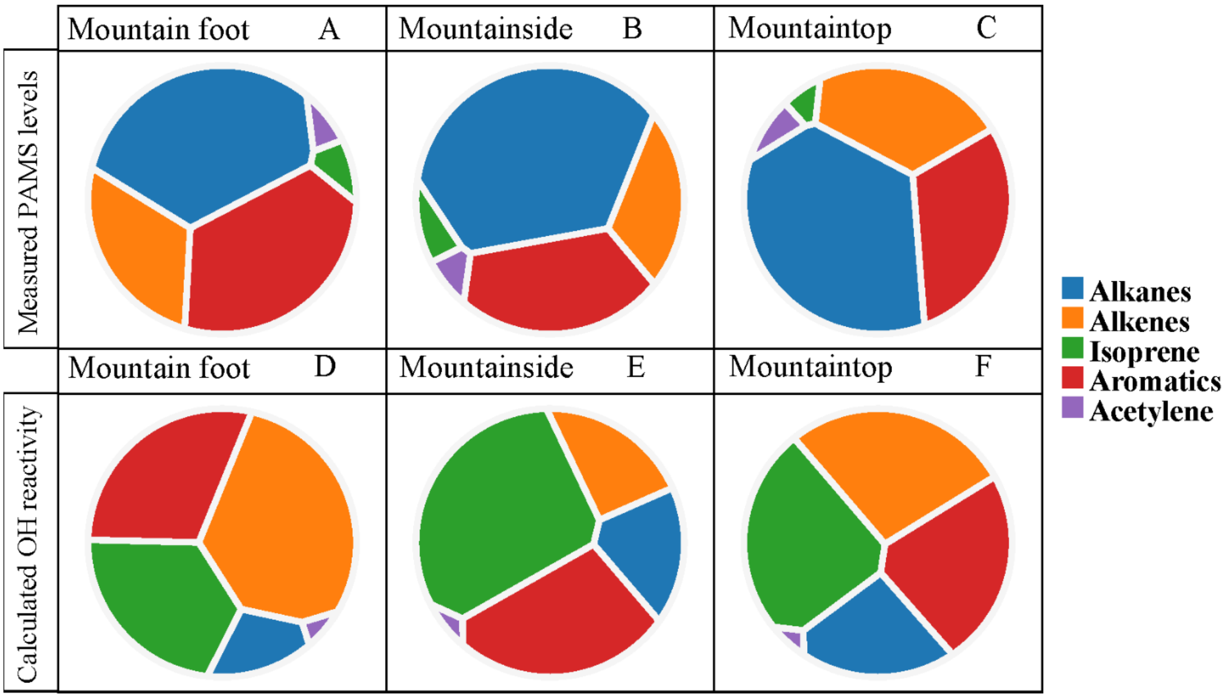

Figure S6. Comprehensive analysis of measured VOCs species concentrations and calculated OH reactivity throughout the campaign period. The mean measured VOCs concentrations were 12.8, 5.1, and 9.4 ppb recorded at the mountain foot, mountainside, and mountaintop sites, respectively. Similarly, the total calculated OH reactivity were 4.4, 1.5, and 2.0 s^{-1} observed at the respective elevation sites.

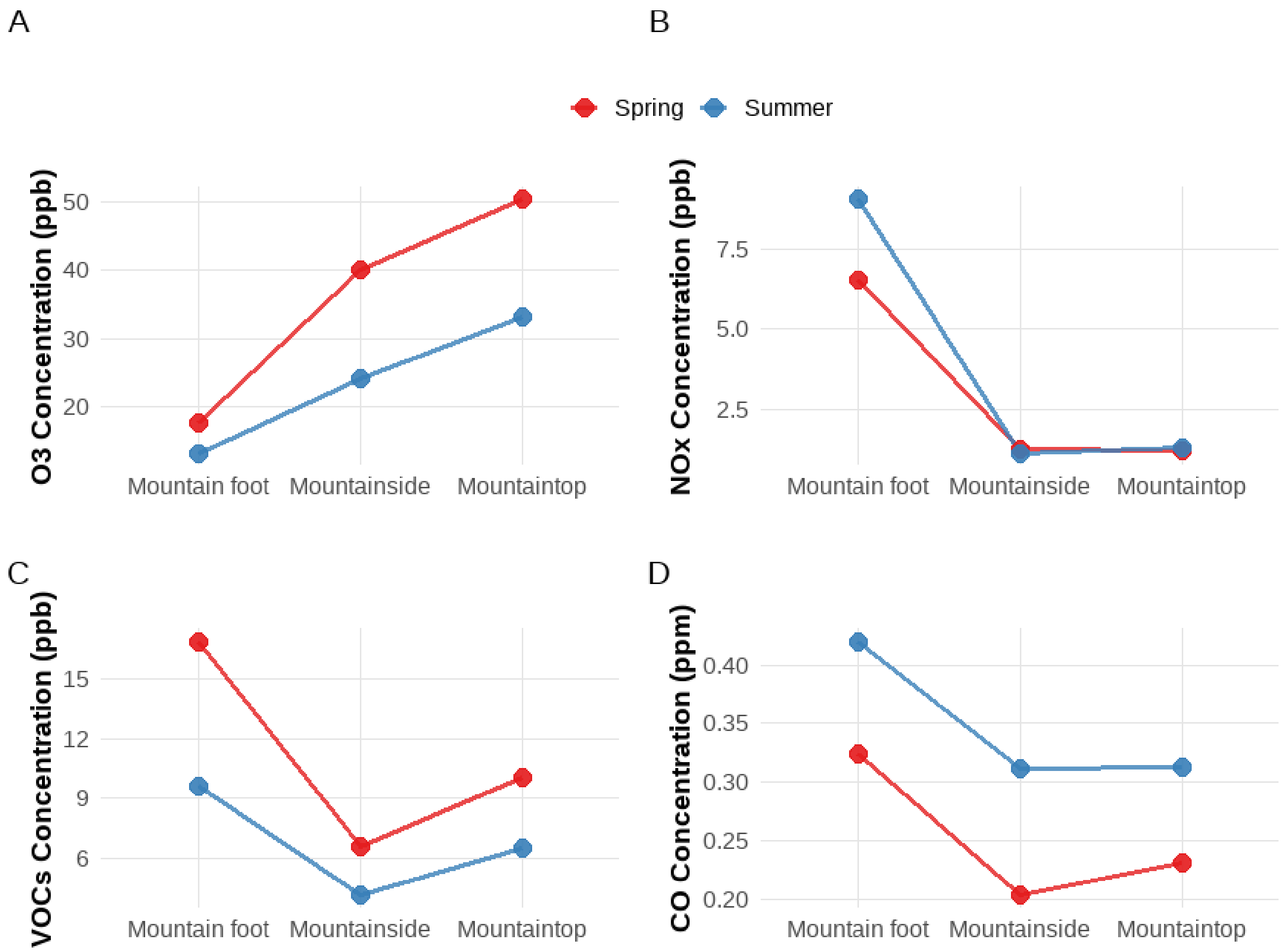

Figure S7. Seasonal and altitudinal variations in air pollutant concentrations across a mountain gradient. The figure comprises four panels (A–D) illustrating mean concentrations of (A) O_3, (B) NOx, (C) VOCs, and (D) CO measured at three elevations (mountain foot, mountainside, and mountaintop) during spring and summer.

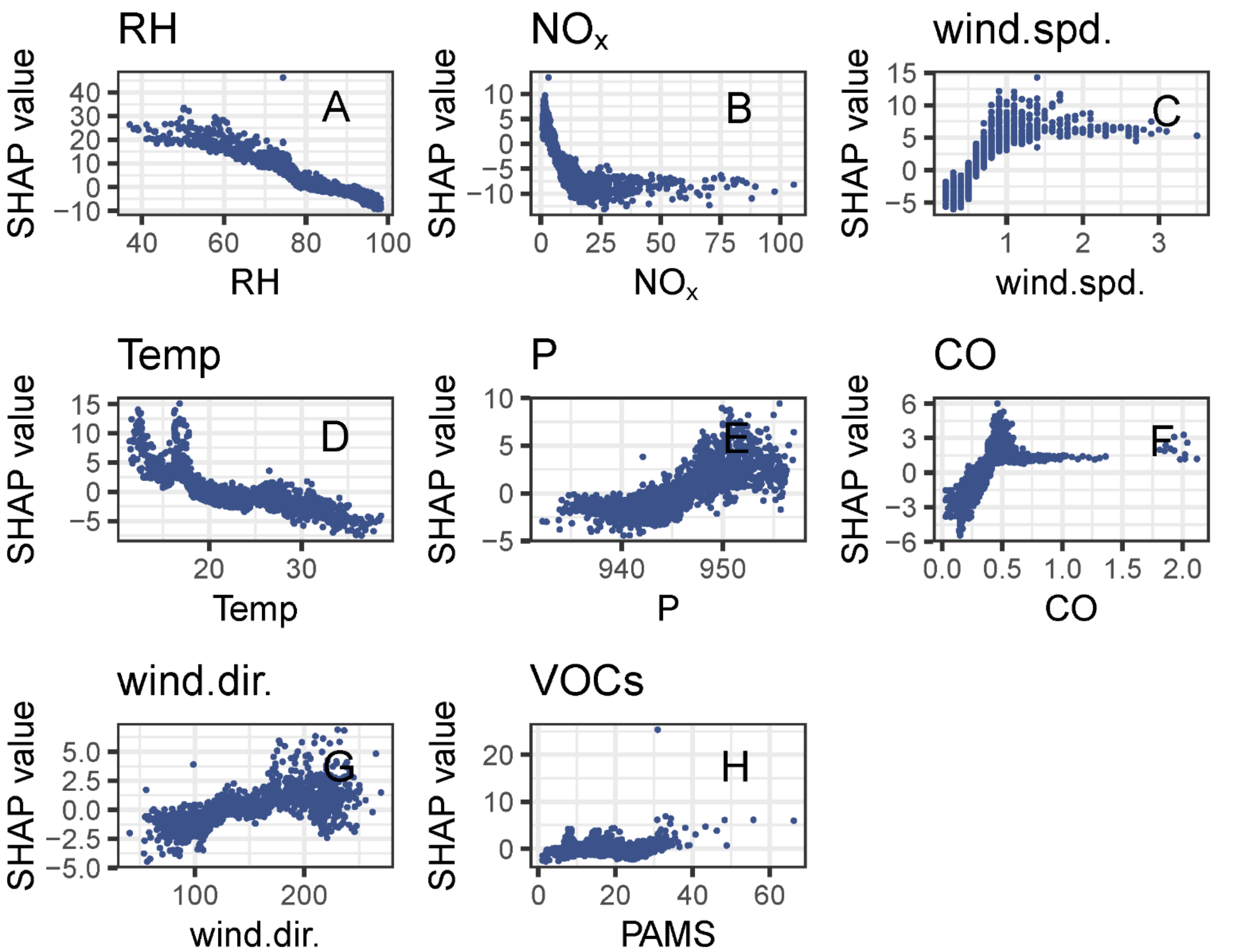

Figure S8. SHAP dependence plot of each feature at mountain-foot O_3 and precursor monitoring station, elucidating the relationship between feature magnitude and SHAP values, providing a clear visualization of how individual features contribute to model predictions.

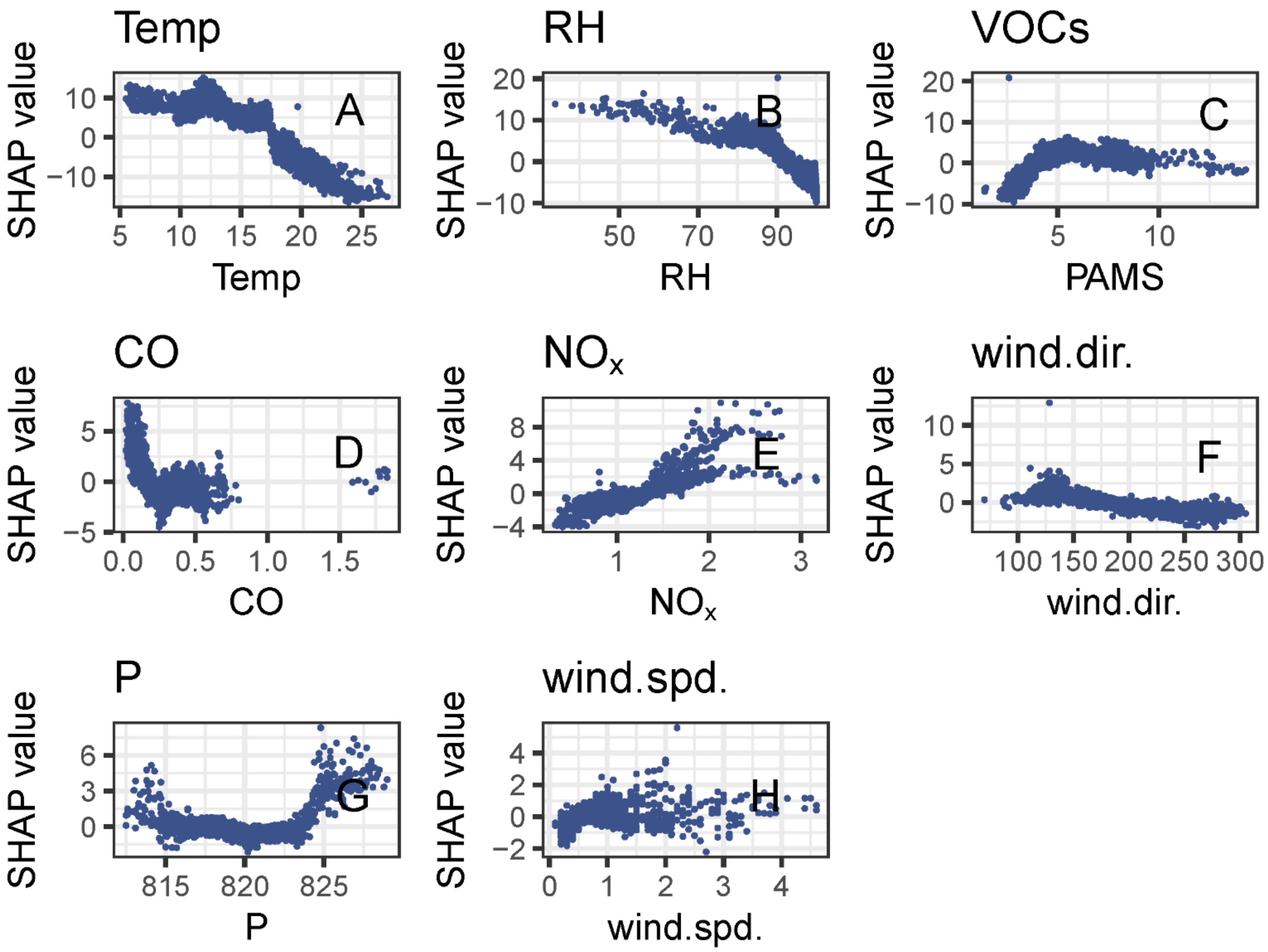

Figure S9. SHAP dependence plot of each feature at mountainside O_3 and precursor monitoring station, elucidating the relationship between feature magnitude and SHAP values, providing a clear visualization of how individual features contribute to model predictions.

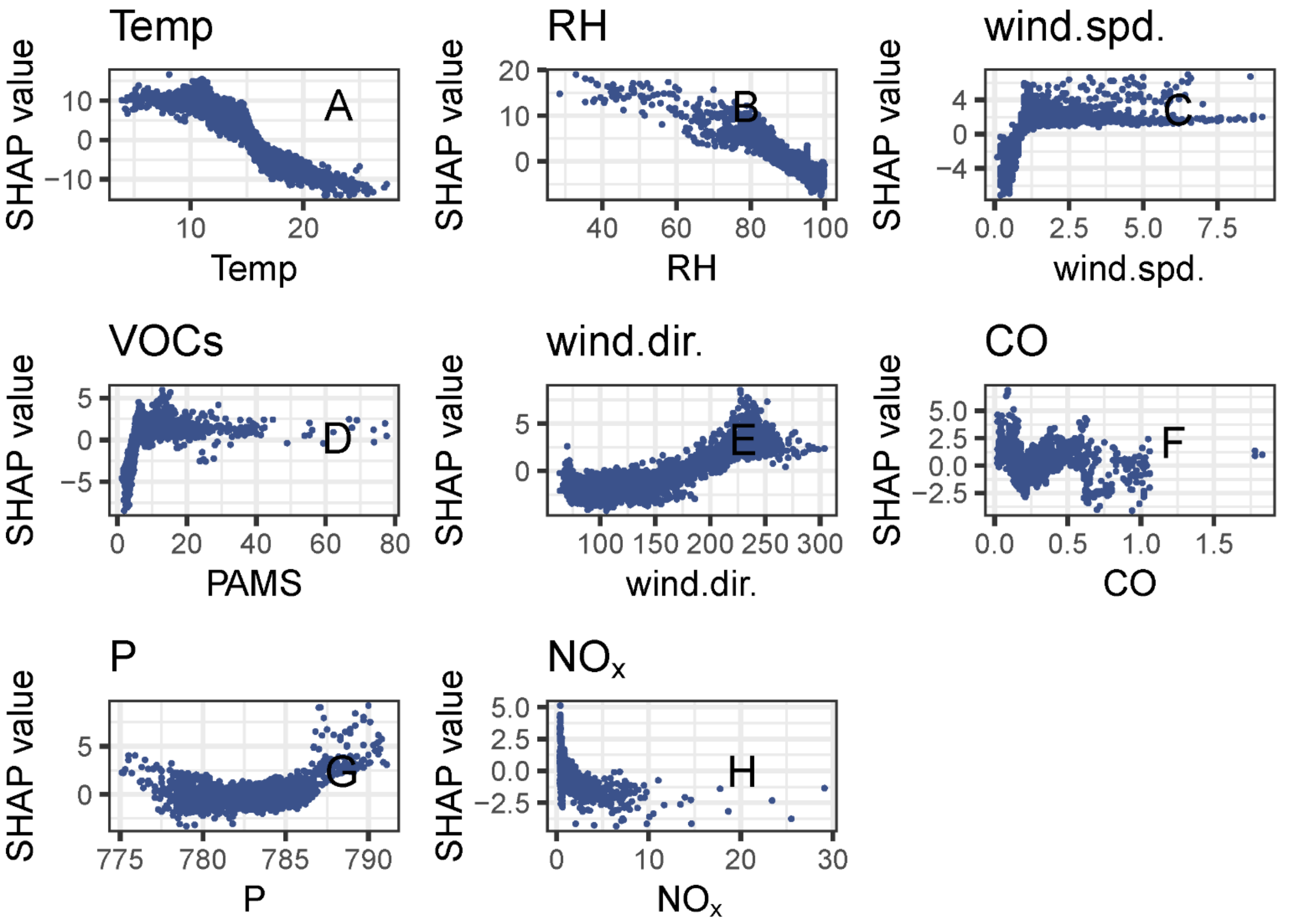

Figure S10. SHAP dependence plot of each feature at mountaintop O_3 and precursor monitoring station, elucidating the relationship between feature magnitude and SHAP values, providing a clear visualization of how individual features contribute to model predictions.

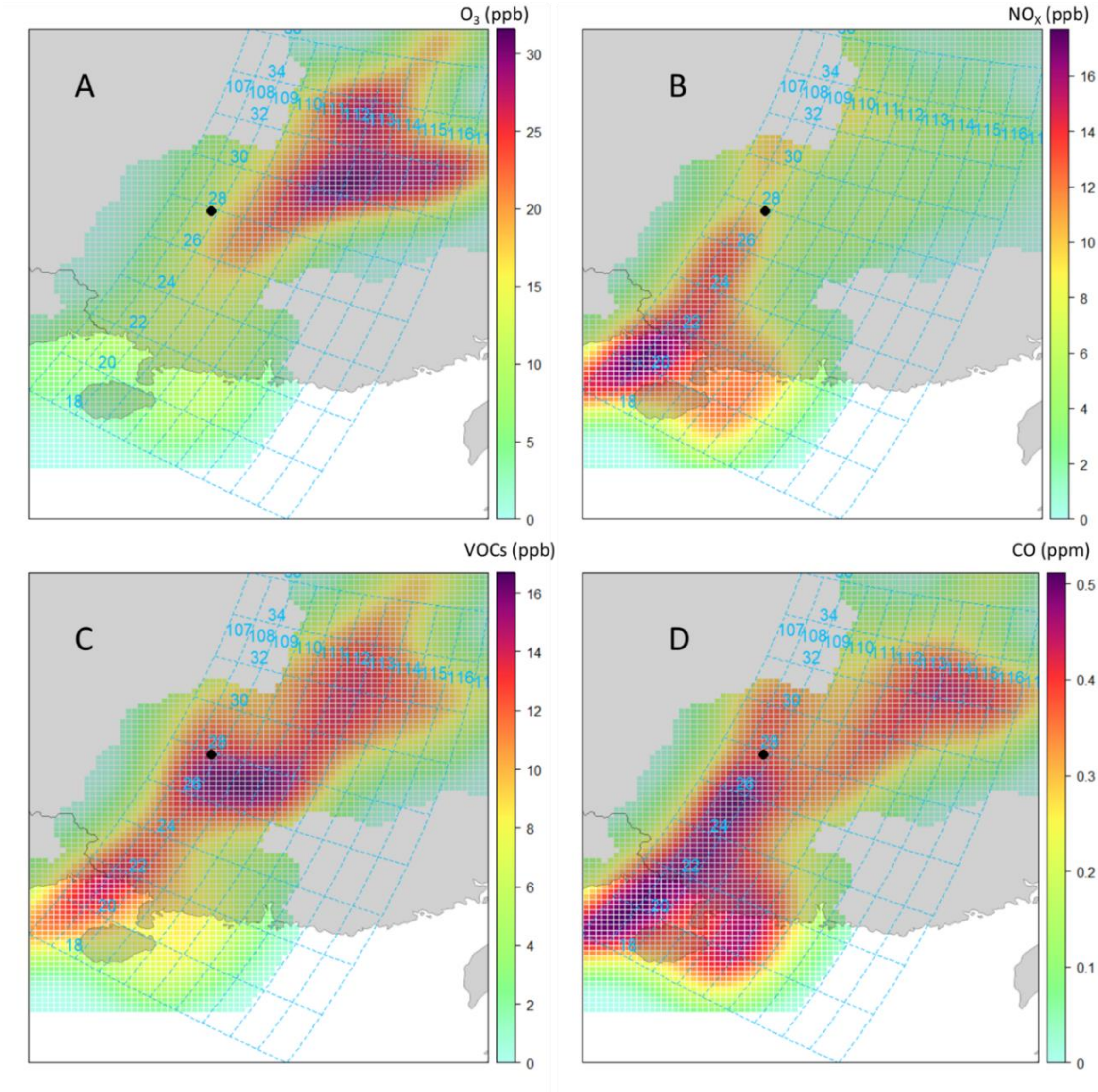

Figure S11. Concentration-weighted trajectory (CWT) plots of O_3 and its precursors at mountain foot throughout the entire observational campaign. The geographical distribution of sampling locations is indicated by solid black markers.

References

Atkinson, R. and Arey, J.: Atmospheric Degradation of Volatile Organic Compounds., Chemical Reviews, 103, 4605-4638, 10.102/cr0206420, 2003.

Atkinson, R., Baulch, D. L., Cox, R. A., Crowley, J. N., Hampson, R. F., Hynes, R. G., Jenkin, M. E., Rossi, M. J., Troe, J., and Subcommittee, I.: Evaluated kinetic and photochemical data for atmospheric chemistry: Volume II – gas phase reactions of organic species, Atmospheric Chemistry and Physics, 6, 3625-4055, 10.5194/acp-6-3625-2006, 2006.

Gong, D., Wang, H., Zhang, S., Wang, Y., Liu, S. C., Guo, H., Shao, M., He, C., Chen, D., He, L., Zhou, L., Morawska, L., Zhang, Y., and Wang, B.: Low-level summertime isoprene observed at a forested mountaintop site in southern China: implications for strong regional atmospheric oxidative capacity, Atmospheric Chemistry and Physics, 18, 14417-14432, 10.5194/acp-18-14417-2018, 2018.

Li, J., Wang, Z., Akimoto, H., Gao, C., Pochanart, P., and Wang, X.: Modeling study of ozone seasonal cycle in lower troposphere over east Asia, Journal of Geophysical Research: Atmospheres, 112, 10.1029/2006JD008209, 2007.

Ling, Z. H., Guo, H., Lam, S. H. M., Saunders, S. M., and Wang, T.: Atmospheric photochemical reactivity and ozone production at two sites in Hong Kong_ Application of a Master Chemical Mechanism–photochemical box model, Journal of Geophysical Research: Atmospheres, 119, 10567-10582, 10.1002/2014jd021794, 2014.

Lyu, X., Guo, H., Zhang, W., Cheng, H., Yao, D., Lu, H., Zhang, L., Zeren, Y., Liu, X., Qian, Z., and Wang, S.: Ozone and its precursors in a high-elevation and highly forested region in central China: Origins, in-situ photochemistry and implications of regional transport, Atmospheric Environment, 259, 118540, 10.1016/j.atmosenv.2021.118540, 2021.

Okamoto, S. and Tanimoto, H.: A review of atmospheric chemistry observations at mountain sites, Progress in Earth and Planetary Science, 3, 10.1186/s40645-016-0109-2, 2016.

Sun, L., Xue, L., Wang, T., Gao, J., Ding, A., Cooper, O. R., Lin, M., Xu, P., Wang, Z., Wang, X., Wen, L., Zhu, Y., Chen, T., Yang, L., Wang, Y., Chen, J., and Wang, W.: Significant increase of summertime ozone at Mount Tai in Central Eastern China, Atmospheric Chemistry and Physics, 16, 10637-10650, 10.5194/acp-16-10637-2016, 2016.

Whalley, L. K., Stone, D., Bandy, B., Dunmore, R., Hamilton, J. F., Hopkins, J., Lee, J. D., Lewis, A. C., and Heard, D. E.: Atmospheric OH reactivity in central London: observations, model predictions and estimates of in situ ozone production, Atmospheric Chemistry and Physics, 16, 2109-2122, 10.5194/acp-16-2109-2016, 2016.

Xu, W., Lin, W., Xu, X., Tang, J., Huang, J., Wu, H., and Zhang, X.: Long-term trends of surface ozone and its influencing factors at the Mt Waliguan GAW station, China – Part 1: Overall trends and characteristics, Atmospheric Chemistry and Physics, 16, 6191-6205, 10.5194/acp-16-6191-2016, 2016.

Yang, Y., Shao, M., Wang, X., Nölscher, A. C., Kessel, S., Guenther, A., and Williams, J.: Towards a quantitative understanding of total OH reactivity: A review, Atmospheric Environment, 134, 147-161, 10.1016/j.atmosenv.2016.03.010, 2016.